TU Delft

Delft University of Technology

Drag, lift and torque acting on a two-dimensional non-spherical particle near a wall

Zarghami, Ahad; Padding, Johan T.

DOI
10.1016/j.apt.2018.03.019

Publication date
2018

Document Version
Final published version

Published in
Advanced Powder Technology

Citation (APA)
Zarghami, A., & Padding, J. T. (2018). Drag, lift and torque acting on a two-dimensional non-spherical particle near a wall. *Advanced Powder Technology*, *29*(6), 1507-1517. https://doi.org/10.1016/j.apt.2018.03.019

Important note
To cite this publication, please use the final published version (if applicable).
Please check the document version above.

Copyright
Other than for strictly personal use, it is not permitted to download, forward or distribute the text or part of it, without the consent of the author(s) and/or copyright holder(s), unless the work is under an open content license such as Creative Commons.

Takedown policy
Please contact us and provide details if you believe this document breaches copyrights.
We will remove access to the work immediately and investigate your claim.

This work is downloaded from Delft University of Technology.
For technical reasons the number of authors shown on this cover page is limited to a maximum of 10.

Advanced Powder Technology 29 (2018) 1507–1517

Contents lists available at ScienceDirect

Advanced Powder Technology

journal homepage: www.elsevier.com/locate/apt

Original Research Paper

Drag, lift and torque acting on a two-dimensional non-spherical particle near a wall

Ahad Zarghami *, Johan T. Padding

Department of Process and Energy, Delft University of Technology, Delft, The Netherlands

ARTICLE INFO

Article history:
Received 23 January 2018
Received in revised form 8 March 2018
Accepted 15 March 2018
Available online 27 March 2018

Keywords:
Lift
Drag
Torque
Non-spherical particle
Wall-effect

ABSTRACT

Gas-solid granular flows with non-spherical particles occur in many engineering applications such as fluidized beds. Such flows are usually contained by solid walls and always some particles move close to a wall. The proximity of a wall considerably affects the flow fields and changes the hydrodynamic forces and torque acting on particles moving near the wall. In this paper, we numerically investigate the drag, lift and torque acting on a non-spherical particle in the vicinity of a planar wall by means of lattice Boltzmann simulations. To gain an exhaustive understanding of the complex hydrodynamics and study the influence of various geometrical and flow parameters, a single 2D elliptical particle is selected as our case study. In the simulations, the effect of particle Reynolds number, distance to the wall, orientation angle and aspect ratio on drag, lift and torque is studied. Our study shows that the presence of a wall causes significant changes in hydrodynamic forces, with increasing or decreasing drag and lift forces, depending on the distance from the wall. Even the direction of lift and torque may change, depending on both the distance from the wall and particle orientation angle. Also, an ellipse with higher AR experiences larger hydrodynamic forces and torque whatever the gap size and orientation angle.
© 2018 The Society of Powder Technology Japan. Published by Elsevier B.V. and The Society of Powder Technology Japan. All rights reserved.

1. Introduction

Granular systems, i.e. assemblies of solid, macroscopic particles, are worth studying because they are commonly encountered in various engineering applications in the energy, chemical and agricultural industries [1–5]. Hence, understanding the characteristics and hydrodynamics of granular materials in a fluid flow is of great importance to increase the efficiency of these applications.

It has been shown that the shape of a particle is one of the most important parameters influencing the hydrodynamics of a granular system [5,6]. It is believed that a significant fraction (estimated around 70%) of processed granular materials have non-spherical shape [5,7]. However, in many studies that deal with granular systems, particles are assumed to be perfect spheres [8–10] due to the fact that the shape characterization of non-spherical particles is a complex process, with various aspects, such as roundness, aspect ratio, irregularity and sphericity, influencing the hydrodynamics [11,12]. Despite much research on hydrodynamics of non-spherical granular particles [5,13–16], significant efforts are still required to accurately predict the hydrodynamic forces acting on non-spherical particles under various flow conditions.

In engineering equipment with granular particles, such as fluidized beds, some of the particles move in the vicinity of a wall. The presence of the wall will change the drag force acting on those particles and, more importantly, the particles experience a transverse lift force known as wall-induced lift [17]. The wall-induced lift is caused by two different competing mechanisms [18,19]. First, the presence of a wall breaks the symmetry of the generated wakes behind the particle which generally results in an effective lift force directed away from the wall. Second, flow relative to the particle will accelerate faster in the gap between the particle and the wall. According to inviscid theory, the pressure in the gap decreases resulting in a lift force directed toward the wall. The wall effect on hydrodynamic forces decays rapidly as the distance between the particles and wall increases, and for distances of the order of 10 (spherical) particle diameters, the wall effect can be reasonably ignored [20].

Investigations of the effect of wall proximity on hydrodynamic forces, i.e. drag and lift forces and torque, acting on non-spherical particles are scarce [21,22] and most of the research work available in the literature is limited to spherical particles [9,10,17,19,23–25]. The purpose of this paper is to investigate the effect of wall

* Corresponding author at: Department of Process and Energy, TU Delft, Leeghwaterstraat 39, 2628CD Delft, The Netherlands.
E-mail address: a.zarghami-1@tudelft.nl (A. Zarghami).

https://doi.org/10.1016/j.apt.2018.03.019
0921-8831/© 2018 The Society of Powder Technology Japan. Published by Elsevier B.V. and The Society of Powder Technology Japan. All rights reserved.

proximity on hydrodynamic forces and torque acting on non-spherical particles in a shear flow up to moderate Reynolds number. In order to gain a better understanding of the complex hydrodynamics, a single two-dimensional elliptic particle is selected as a case study. The effect of flow Reynolds number, gap size (or minimum separation distance from the wall), and orientation on drag and lift forces are studied. For this purpose, the lattice Boltzmann method (LBM) is applied as a capable and accurate technique for simulating the fluid flow.

The rest of this paper in organized as following. In Section 2, the numerical method is presented briefly. Results and discussions are presented in Section 3, follow by concluding remarks in Section 4.

2. Numerical method

2.1. LBM for fluid flow

In In the past two decades the LBM, a mesoscopic numerical method based on kinetic theory [26], has become an alternative, capable and computationally efficient technique for simulating various complex fluid flows [27–29]. The simple form of the governing equations, space–time locality, straightforward parallelism, easy grid generation and capability of incorporating complex microscopic interactions are the main advantages of LBM compared with conventional CFD methods based on Navier–Stokes equations. The general lattice Boltzmann equation with the BGK collision operator is expressed as [26]:

$$\frac{f_i(\vec{x}+\vec{e}_i\Delta t, t+\Delta t)-f_i(\vec{x},t)}{\Delta t} = -\frac{1}{\tau}\left(f_i(\vec{x},t)-f_i^{eq}(\vec{x},t)\right) \tag{1}$$

where $\vec{x}$ is a spatial coordinate, t is time, $f_i(\vec{x},t)$ is the density distribution function associated with discrete velocity direction i, and τ is the relaxation time of the fluid. The discrete velocities $\vec{e}_i$ in the ith-direction, for the D2Q9 lattice are given by $\vec{e}_0 = 0$ and $\vec{e}_i = \lambda_i(\cos\theta_i, \sin\theta_i)$ with $\lambda_i = 1, \theta_i = (i-1)\pi/2$ for $i = 1{-}4$ and $\lambda_i = \sqrt{2}, \theta_i = (i-5)\pi/2 + \pi/4$ for $i = 5{-}8$. The order number $i = 1{-}4$ and $i = 5{-}8$ represent the rectangular and the diagonal directions of the lattice, respectively. Also, f_i^{eq} is the equilibrium distribution function, defined as:

$$f_i^{eq} = w_i\rho\left[1+\frac{(\vec{e}_i\cdot\vec{u})}{c_s^2}+\frac{(\vec{e}_i\cdot\vec{u})^2}{2c_s^4}-\frac{(\vec{u}\cdot\vec{u})}{2c_s^2}\right] \tag{2}$$

where $c_s = 1/\sqrt{3}$ is the lattice speed of sound, $\vec{u}$ is the velocity, and w_i are the weighting factors, equal to 4/9 for $i = 0$, 1/9 for $i = 1{-}4$ and 1/36 for $i = 5{-}8$. The local mass density, the viscosity, velocity and the pressure in lattice units are calculated as $\rho = \sum_i f_i$, $v = (\tau - 0.5)/3$, $\vec{u} = (\sum_i \vec{e}_i f_i)/\rho$ and $p = \rho c_s^2$, respectively.

Eq. (1) is usually solved through standard collision and streaming steps as:

$$\text{Collision}: \tilde{f}_i(\vec{x}, t+\Delta t) = f_i(\vec{x},t) - \frac{\Delta t}{\tau}\left(f_i(\vec{x},t)-f_i^{eq}(\vec{x},t)\right) \tag{3}$$

$$\text{Streaming}: f_i(\vec{x}+\vec{e}_i\Delta t, t+\Delta t) = \tilde{f}_i(\vec{x}, t+\Delta t) \tag{4}$$

where $\tilde{f}_i$ represents the post-collision state. The simulation is performed on a square Cartesian grid where for convenience dimensionless lattice units are utilized, i.e. $\Delta\vec{x} = \Delta t = 1$. During the streaming step the particles move from a node to its neighbor node, according to the set of discrete velocities. Computationally speaking, during the streaming step all distribution functions are copied to the adjacent node in the direction of the lattice vector. Therefore, the streaming step involves very little computational effort. During the collision step the particles relax towards local equilibrium according to the collision operator.

In this research for computing the fluid force on a body, the momentum exchange approach [30] after the streaming step is applied:

$$\vec{F} = \sum_{all\ x_b}\sum_{i=1}^{8}\vec{e}_{\bar{i}}\left[\tilde{f}_i(\vec{x}_b,t)+\tilde{f}_{\bar{i}}(\vec{x}_f,t)\right] \tag{5}$$

where $\bar{i} = -i$ and the summation is done over all boundary nodes $\vec{x}_b$, which are connected to a fluid node in the i direction according to $\vec{x}_b = \vec{x}_f + \vec{e}_i\Delta t$ (see Fig. 1).

2.2. No-slip boundary condition

One important and outstanding issue in the LBM is that of solid boundary conditions needed to effectively model the interactions between fluid flow and a solid wall. In LBM, the boundary conditions influence the accuracy and stability of the computation. In the conventional CFD methods, the boundary conditions are defined using macroscopic variables (such as velocity), whereas in the LBM, the boundary conditions are enforced by changing the distribution functions, but no physically based boundary constraints for the distribution functions are provided. Therefore compared to traditional CFD methods, the LBM suffers from unknown variables at boundaries. In other words, the difficulty of applying boundary conditions in the LBM is to determine the particle distribution functions leaving into the fluid domain, but which originate from outside the bulk fluid domain (e.g. solid walls).

Fig. 1 depicts the schematic of the wall boundary condition for a one-dimensional arbitrary shaped moving object between the lattice nodes of spacing Δx. Because a no-slip boundary with a non-moving wall can be modelled by mirroring the fluxes at the boundary along each possible velocity directions separately, for one dimension it is sufficient to only consider a one-dimensional projection of lattice direction with its intersection with a (curved) wall boundary surface at x_w. The curved-wall boundary may be located at an arbitrary position between the solid and fluid nodes (i.e. x_b and x_f). The fraction of an intersected link in the fluid region is expressed using a parameter q as $q = (x_w - x_f)/\Delta x$. Obviously, $0 \leqslant q \leqslant 1$ and the distance between x_b and x_w is $q\Delta\vec{x}$.

We model the surface of a non-spherical particle as a no-slip boundary, using the so-called Bouzidi scheme [31]. Bouzidi et al. [31] proposed a method with second-order accuracy that does not require the extrapolations from the ghost nodes in solid wall. The Bouzidi scheme combines the bounce-back concept with quadratic interpolation of the distribution functions from the internal fluid nodes. For $q < 0.5$:

$$\tilde{f}_{\bar{i}}(x_f, t+\Delta t) = q(1+2q)\tilde{f}_i(x_f,t) + (1-4q^2)\tilde{f}_{\bar{i}}(x_{ff},t) - q(1-2q)\tilde{f}_{\bar{i}}(x_{fff},t) \tag{6}$$

and for $q \geqslant 0.5$:

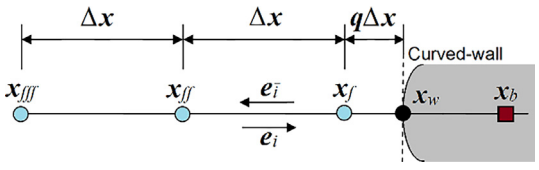

Fig. 1. One-dimensional representation of a regular lattice and a curved-wall boundary.

$$\widetilde{f}_i(x_f, t+\Delta t) = \frac{1}{q(1+2q)}\widetilde{f}_i(x_f, t) + \frac{2q-1}{q}\widetilde{f}_i(x_f, t) - \frac{2q-1}{2q+1}\widetilde{f}_i(x_{ff}, t) \quad (7)$$

It is worth mentioning that, form a coding perspective, when using the curved boundary schemes, it is more efficient to combine collision and streaming to one step. Because streaming simply corresponds to shifts of indices labelling spatial nodes of f_i, this means that: $\widetilde{f}_i(x_b, t) = \widetilde{f}_i(x_f, t+1)$ or $\widetilde{f}_i(x_{ff}, t) = \widetilde{f}_i(x_f, t+1)$ and so on. Therefore, the curved boundary schemes can be re-written without involving the after-collision distribution function $\widetilde{f}_i$.

It is well-known that the exact location of the no-slip boundary is viscosity-dependent when bounce back or interpolation schemes are used together with the BGK collision model and the plane of zero velocity is not exactly located halfway along the link for flows with varying velocity gradients [26,32,33]. This implies that the hydrodynamic solution will differ for the same grid at different viscosities, even though the governing physical parameters of the problem, e.g. Reynolds number, are fixed. The reason is that the relaxation time simultaneously controls the fluid viscosity and the discretisation errors. Hence, solutions obtained with the BGK model generally exhibit τ-dependent and therefore viscosity-dependent characteristics.

In order to resolve the τ-dependent error, which is also called boundary slip velocity error, several strategies can be adopted. The most general approach is to replace the BGK collision model by the more complex collision models such as MRT model [34]. Note that this boundary slip velocity error is not present in linear solutions, such as Couette flow, and it stems from the $O(\Delta x^2)$ term in the bounce-back closure relation. It means that for fixed values of τ, the boundary slip error decreases with a second-order rate as function of grid resolution [32,33]. Therefore, to guarantee consistent errors across simulations one needs to simultaneously tune the relaxation time, the grid number and, to a smaller extent, the macroscopic velocity. This issue is discussed more in Section 3.1.

2.3. Inlet/outlet boundary condition

The well-known Zou and He boundary condition [35] is used for the inlet boundary. Assuming that the velocity on the inlet boundary $(U_{in}, V_{in} = 0)$ is known, the unknown distribution functions at inlet are given by $f_1 = f_3 + 2\rho_{in}U_{in}/3$, $f_5 = f_7 + 0.5(f_4 - f_2) + \rho_{in}U_{in}/6$ and $f_8 = f_6 + 0.5(f_2 - f_4) + \rho_{in}U_{in}/6$ where $\rho_{in} = [f_0 + f_2 + f_4 + 2(f_3 + f_6 + f_7)]/(1 - U_{in})$.

For the outflow, the convective boundary condition is applied. The convective boundary condition can be written as [36]:

$$\frac{\partial \chi}{\partial t} + U_o\frac{\partial \chi}{\partial x} = 0, \quad x = N \quad (8)$$

where χ is an arbitrary function and where U_o is a typical velocity normal to the outlet boundary which is defined as [37]:

$$U_o = U_{\max}(t) \equiv \max\{u(N-1, j, t)\} \quad (9)$$

where $0 \le j \le M$ and $M+1$ are the number of nodes in the $(N-1)$th layer in the y direction. Note that U_o is time dependent, which is taken from the last time step when one calculates the distribution functions at the outlet. The mesoscopic representative of the convective boundary condition for the unknown distribution functions at outlet boundary located at $x = N$ is expressed as follows [37]:

$$f_i(N, j, t+\Delta t) = \frac{f_i(N, j, t) + \kappa f_i(N-1, j, t+\Delta t)}{1+\kappa} \quad (10)$$

where $\kappa = U(t+\Delta t)$, which is known after the streaming step at the $(N-1)$th layer.

3. Results & discussions

3.1. Problem statement

A schematic of the flow configuration and boundary conditions is shown in Fig. 2(a). The flow enters the computational domain (channel) with a uniform velocity, $(U_{in}, 0)$. No-slip and free-slip boundary conditions are applied to the bottom and top of the channel boundaries, respectively. The length of the channel is L and the upper and lower walls are separated by a distance H. An elliptic particle is placed in the domain with the major and the minor diameters equal to a and b, respectively. Hence, the particle aspect ratio is defined as AR = a/b. The major diameter of the ellipse is fixed $a = 50$ lattice nodes, and the size of the computational domain is set $H = N_y = 12a = 600$ and $L = N_x = 14a = 700$ (for $Re < 50$) or $L = N_x = 25a = 1250$ (for $Re \ge 50$) lattice nodes. The particle orientation with respect to the main flow direction (**x** axis) is defined by θ. The minimum distance (or gap size) between the particle surface and wall is indicated by h ranging from $a/20$ (≈3 lattice nodes) to $8a$ (400 lattice nodes).

The Reynolds number is defined as $Re = U_{in}D/\nu$, where $D = (ab)^{0.5}$ is the equivalent diameter of the elliptical cylinder. In this paper, the relaxation time is fixed $\tau = 0.56$ for all presented simulations. Considering the fixed size of the ellipse in all simulations, various Re numbers are obtained by varying the fluid velocity, U_{in}.

The location of the center of the ellipse, X_o, from the inlet boundary may have an important effect on the hydrodynamics of the flow field. Fig. 2(b) shows that the drag force acting on an ellipse with AR = 4 decreases monotonically, for all presented gap sizes, as the ellipse center is placed further from the inlet boundary. This behavior is more evident when the gap size, h, becomes smaller. However, the drag force remains almost constant when

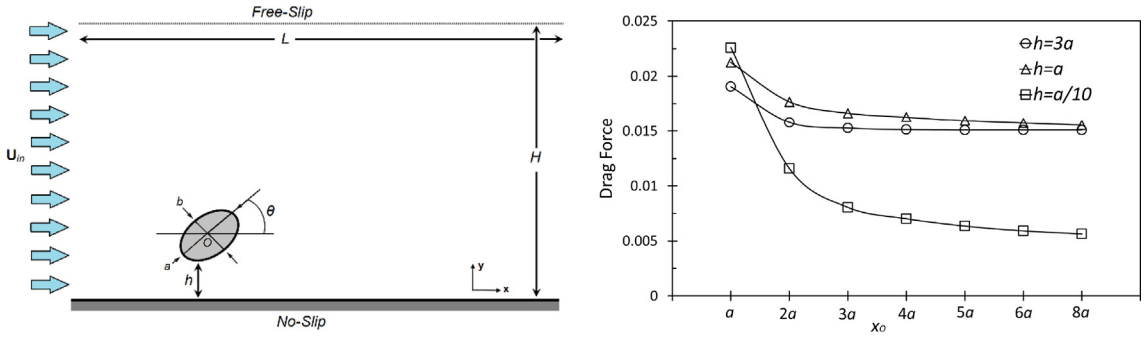

Fig. 2. (a) Schematics of shear flow around an elliptic particle close to a wall and (b) effect of horizontal displacement of the ellipse center, X_O, on drag force for AR = 4 and different gap sizes.

X_O is far enough from the inlet boundary. The results show that the maximum difference between $X_O = 5a$ and $X_O = 8a$ is not significant, so we use $X_O = 5a$ as the location of the center of the ellipse in this study. Hence, the outlet boundary is truncated at $20a$ from the ellipse center to avoid boundary effects on the development of wakes behind the particle.

It is worth mentioning that the boundary layer thickness of wall, δ, can be calculated as $\delta/a = \sqrt{\pi X_O/aRe}$ [38]. Considering $X_O = 5a$, the wall boundary layer thickness for $Re = 5$, 25 and 100 is $1.7a$, $0.6a$ and $0.4a$, respectively. Hence, we can conclude that the particle will cross the wall boundary layer when the gap size becomes small. For example, the particle in the flow with $Re = 5$ will be completely out of the wall boundary layer if $h = 3a$, will cross the wall boundary layer if $h = a/2$ and will be completely inside the wall boundary layer if $h < 0.7a$. However, the wall boundary layer thickness at $Re = 100$ and $X_O = 5a$ is smaller than the major diameter of the particle, a, hence it is obvious that the particle only cross the boundary layer when h is very small and never is placed inside the boundary layer.

It can be shown that the slip velocity error can be kept small for τ close to $\Delta t/2$, and on the contrary, for larger relaxation times, the error becomes unacceptably large. A similar geometry to our case study is Poiseuille flow, which can be used to obtain an approximation to the error for our work. The effective width of the channel in lattice units, H_{eff}, for a Poiseuille flow in a 2D lattice-aligned channel is given by: $H_{\text{eff}}^2 = N_y^2 + 48\nu^2 - 1$ [39], where N_y is the number of lattice points across the channel and ν is the viscosity in lattice units. Typically at $Re > 1$ the larger system sizes and smaller relaxation times combine to reduce the relative error. As we mentioned earlier, we fix the relaxation time $\tau = 0.56$ for all presented simulations which results in $\nu = 0.02$. Considering the number of lattice nodes in the cross-stream direction, i.e. $N_y = 700$, the effective width is $H_{eff} = 699.8$, a relative error less than 0.01%. Hence, the slip velocity error could be ignored in our study.

3.2. Numerical results

In this section, the effect of various effective parameters, i.e. gap size, *Re* number, orientation and AR on hydrodynamic forces acting on the particle are presented.

3.2.1. Gap size effect

In order to show the effect of gap size on hydrodynamic forces we focus on an elliptic particle with AR = 3 and $\theta = 0°$. Figs. 3 and 4 show the streamlines around the ellipse at various gap size for $Re = 5$ and 25, respectively. These figures are for $h = 3a$, $h = a$, $h = a/5$ and $h = a/20$. Since the *Re* number for both cases is small, the flow around the ellipse remains attached when particle is far from the wall (i.e. for $h = 3a$ and $h = a$). As the distance from the wall increases, the symmetry in streamlines becomes more evident. By decreasing the gap size the effect of the wall on the hydrodynamics of flow is pronounced. For $h = a/5$, the gap flow increases both in terms of velocity and mass flow rate and a free jet is formed. As a result, a downstream recirculation region is generated. It can be seen that the recirculation region for $h = a/5$ is slightly away from the particle, which is possibly due to strong gap flow. At the smallest presented gap size, i.e. $h = a/20$, the gap flow becomes weaker. Keeping in mind the relatively thick boundary layer at the particle's position, a weak gap flow is expected. In this case, the ellipse forms an obstacle to the approaching flow, a recirculation region is formed very close to the particle and most of the fluid is directed over the top of the particle.

The dependence of the drag and lift forces on the gap size for both $Re = 5$ and 25 are presented in Fig. 5. It can be seen that the drag force is a constant value when the particle is far from the wall and then increases with decreasing the gap size to around $h \approx a$ (for $Re = 5$) and $h \approx a/2$ (for $Re = 25$) due to the effect of the wall. This increase in drag force can be justified in terms of the added viscous effect arising from the presence of the wall. However, by further decreasing the gap size to very small sizes the drag force decreases. The effect of the wall on the flow near an elliptic particle with its longer axis ordinated to the wall (i.e. $\theta = 0°$) is to slow down the gap flow which results in a reduction in viscous friction on the wall facing side of the particle.

A similar trend is observed for the lift force. As we mentioned earlier, the wall-induced lift force is due to two mechanisms. The vorticity generated at the particle surface advects and diffuses downstream, interacts with the wall and results in a lift force directed away from the wall. On the other hand, the fluid is accelerated in the gap between the particle and the wall in the limit of an inviscid flow. This effect results in a local low pressure region in

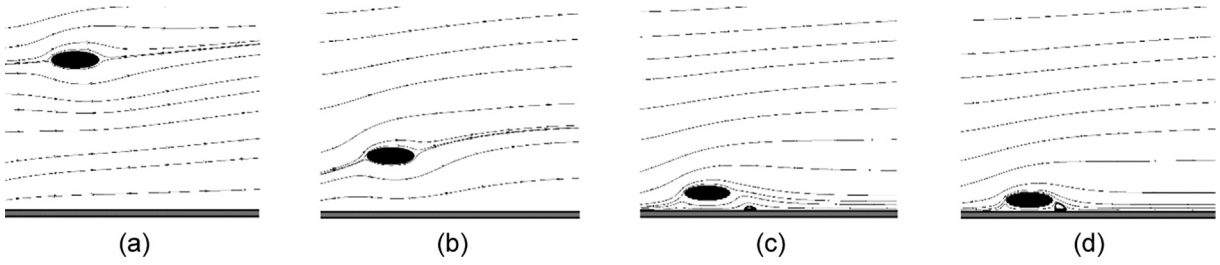

Fig. 3. Flow streamlines around an ellipse with AR = 3, $Re = 5$, $\theta = 0°$ for (a) $h = 3a$, (b) $h = a$, (c) $h = a/5$ and (d) $h = a/20$.

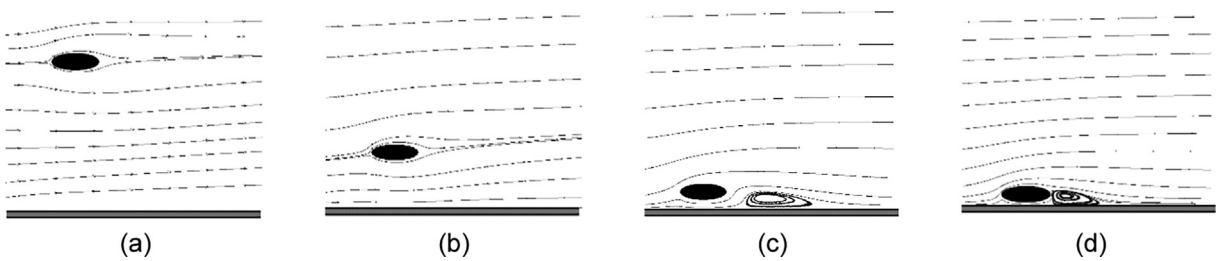

Fig. 4. Flow streamlines around an ellipse with AR = 3, $Re = 25$, $\theta = 0°$ for (a) $h = 3a$, (b) $h = a$, (c) $h = a/5$ and (d) $h = a/20$.

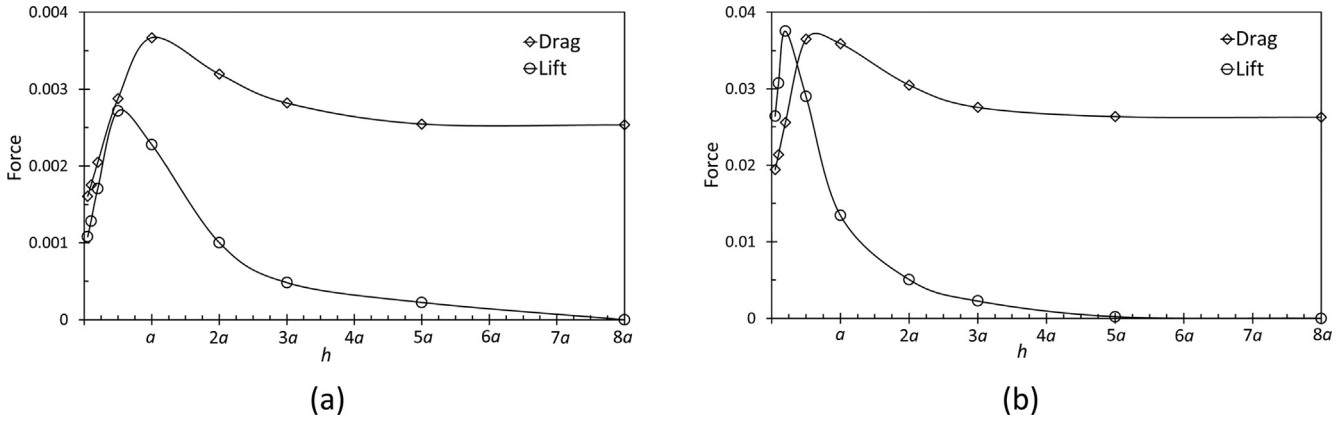

Fig. 5. Drag and lift forces as a function of gap size, h, for an elliptic particle with AR = 3 and $\theta = 0°$ at (a) $Re = 5$ and (b) $Re = 25$.

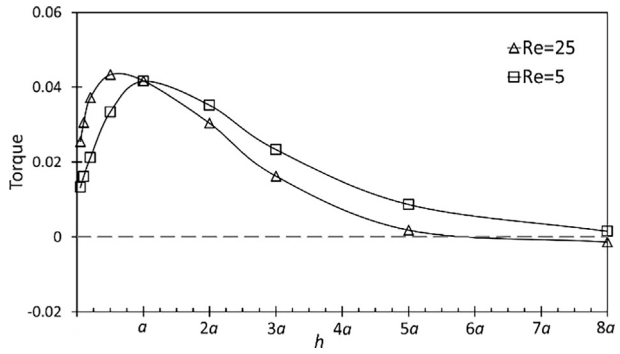

Fig. 6. Rotating torque as a function of gap size, h, for an elliptic particle with AR = 3 and $\theta = 0°$ at $Re = 5$ and $Re = 25$.

the gap that corresponds to a net lift force directed towards the wall. The lift force is zero when the particle is far from the wall. However, by decreasing the gap to $a/2$ (for $Re = 5$) or $a/5$ (for $Re = 25$), the lift force increases significantly. For large gap sizes the effect of wall-directed lift force (with negative sign) is insignificant and the lift force directed away from the wall (with positive sign) is dominant. However, when the particle gets very close to the wall, the wall-directed lift force becomes larger, resulting in a decrease in net lift force.

The torque acting on the particle for both $Re = 5$ and 25 is shown in Fig. 6. It is clear that the torque follows the trends of the drag and lift forces. The torque is close to zero when the particle is far from the wall. From this figure it is evident that the wall tends to increase the torque when the particle gets closer to the wall. The present ellipse with AR = 3 and $\theta = 0°$ in a flow with low Re number behaves like a streamlined bluff body as the boundary layers on the top and bottom surface experience only mild pressure gradients, and they remain attached along almost the entire length. The wake behind the ellipse is very small, and the drag is dominated by the viscous friction inside the boundary layers. As we mentioned earlier, by approaching the wall the wall facing side of the ellipse experiences larger positive viscous drag compared to the upper face, this results in a positive (or counter clockwise rotating) torque acting on the particle. By decreasing the drag and lift forces at very small gap sizes, the torque decreases as well.

3.2.2. Re number effect

Fig. 7 show the streamlines around an elliptic particle with AR = 4, $\theta = 90°$ with $h = 3a$, $a/2$ and $a/20$ at different Re numbers. It can be seen that (see top panels in Fig. 7) when the particle is far from the wall (i.e. at $h = 3a$), the flow around the ellipse closely resembles that of an isolated elliptical cylinder, as two steady and roughly symmetric recirculation regions are formed behind the ellipse at $Re = 5$. By increasing the Re number, the vortex shedding from the upper and lower sides of the particle is started ($Re = 50$) and finally the well-known von-Karman vortex street is formed at $Re = 100$.

It is worth mentioning that the difference in vortex shedding is due to the lower dimensionality. As a matter of fact, a 2D particle (here: an ellipse) may be conceived as infinity long cylinder without any variation in the third direction, whereas it is not the case for a 3D particle (here: an ellipsoid). According to the literature, the wake grows more slowly for this axisymmetric flow around a 3D bluff body than for the planar flow around a 2D cylinder. In general, a 3D body is characterized by lower hydrodynamic loads (such as Drag force) than those acting on a 2D body of analogous cross-shape. This is, in a sense, reasonable, since the disturbance caused by a 3D body is lower due to the possibility of flow in an additional direction. As an example, for flow around a 2D circular cylinder the wake behind the cylinder first becomes unstable to perturbations at a critical Reynolds number of about $Re_{cr} = 46 \pm 1$ (see [40,41]). Above this Reynolds number, a small asymmetric perturbation in the near wake will grow in time and lead to an unsteady wake and Von Karman vortex shedding. However, in contrast to the cylinder, for the 3D sphere wake, the bifurcation leading to a time-dependent flow and vortex shedding occurs near the critical Reynolds number $Re_{cr} = 212$ [42,43].

When the particle gets closer to the wall, i.e. at $h = a/2$ (see middle panels in Fig. 7), the fluid flow structure downstream of the ellipse is strongly affected by the presence of the wall. At $Re = 5$, one single steady recirculation region is formed behind the particle due to the strong gap flow which is like a free jet. By increasing the Re number to 50 the flow becomes unstable and vortices are shed from the cylinder into the wake region behind it. In this case, the sizes of the vortices shed from the upper and lower sides of the ellipse are different due to the effect of the wall, and the vortices shed from the lower side move faster downstream than those shed from the upper side due to the strong gap flow. At $Re = 100$, the vortex region becomes complex and the vortices become larger and migrate away from the cylinder due to the strong gap flow.

At very small gap size (i.e. $h = a/20$), the flow is steady at $Re = 5$ and a recirculation region forms behinds the ellipse. For this very small gap size, the ellipse looks like an obstacle to the fluid flow and by increasing the Re number, the size of the recirculation region behind it increases. At $Re = 100$, a secondary recirculation region is also formed. It is worth mentioning that due to the small gap size and also thick shear layer of the wall at low Re number

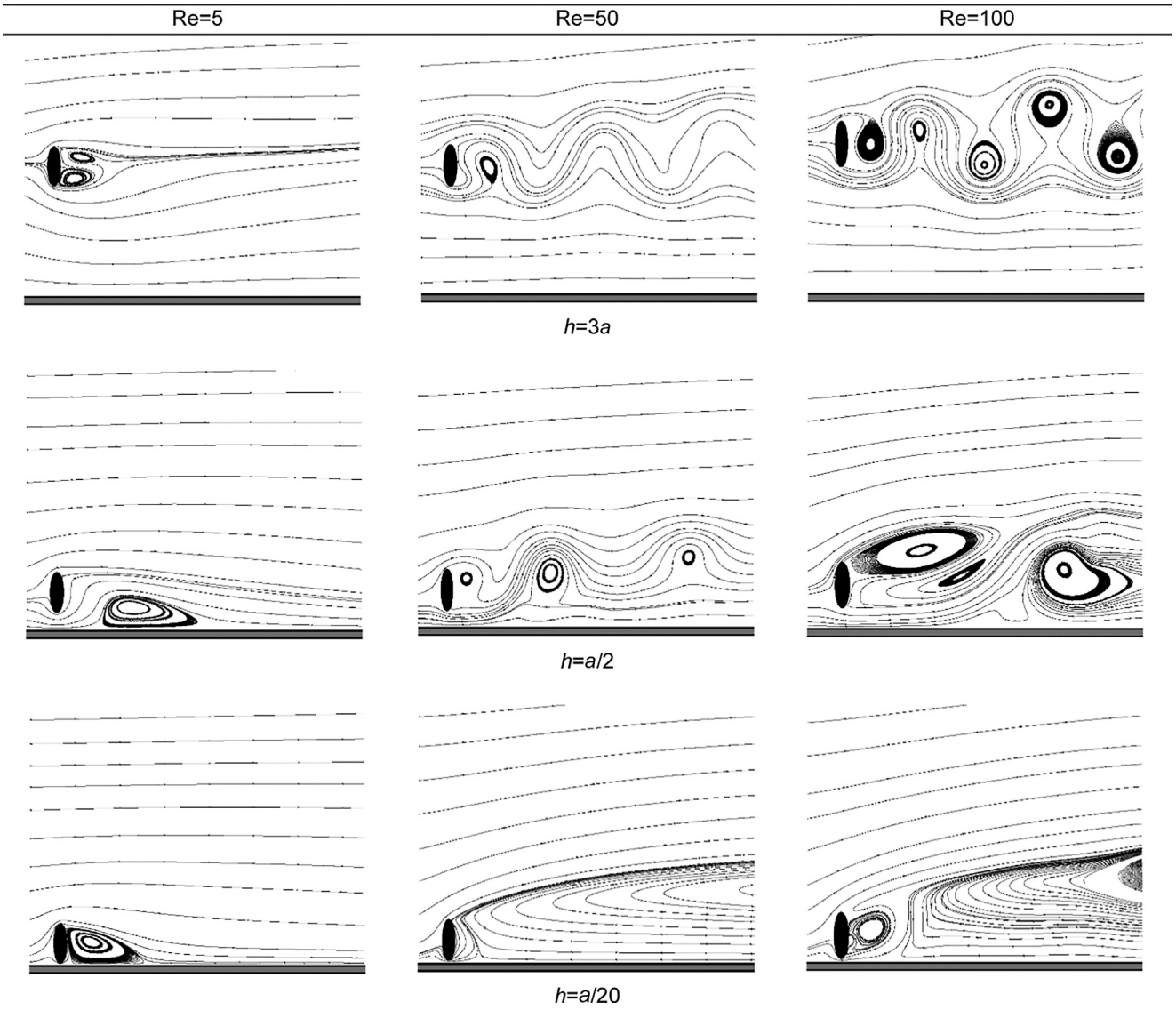

Fig. 7. Flow streamlines around an ellipse with AR = 4, $\theta = 90^\circ$ for various *Re* numbers (columns) and gap widths (rows).

flows, the wall shear layer interacts with the lower shear layer on the ellipse at this gap size. The negative wall shear layer cancels part of the vorticity in the positive lower shear layer, thus the lower shear layer is weakened. Consequently, the separated lower shear layer is not strong enough to roll up to form a vortex, and it is also not strong enough to affect the upper free shear layer. Therefore, the wake development is rather stable and no significant difference can be observed from the vorticity contours during various time periods.

The effect of *Re* number on the time-dependent drag force at different gap sizes is shown in Fig. 8. It can be seen that the drag force depends strongly upon *Re* number. Due to the vortex shedding, the drag force is periodic when the ellipse is far from the wall. When vortex shedding occurs, vortices are shed alternatively from the top and the bottom of the particle. It causes fluctuations in the pressure and flow velocity in the near wake of the ellipse and also generates fluctuating forces on the ellipse. However, the drag force is roughly a constant value when the *Re* is small or when the particle is very close to the wall (see Fig. 8c). As discussed earlier, in this case the ellipse resembles an obstacle to the fluid flow and only one stable recirculation region forms behind it. Also, one can see that when the particle is far from the wall and the flow is periodic, the frequency of vortex shedding increases as the *Re* number becomes larger.

Like the drag force, the wall-induced lift force varies widely with *Re* number and time as shown in Fig. 9. Generally, the averaged wall-induced lift increases with *Re* number. For example, the average of lift forces in Fig. 9(a) are equal to 10^{-3}, 2×10^{-3} and 11×10^{-3} for $Re = 5$, 50 and 100 respectively. Also, it is clear that when the ellipse is located far from the wall (i.e. $h = 3a$), the lift force oscillates regularly due to the vortex shedding phenomena at higher *Re* numbers. By decreasing the gap size to $h = a/2$, a reduction in the amplitude of the fluctuations of the lift coefficient is observed. This reveals that the strength of the vortex shedding is reduced. If the ellipse gets closer to the wall (i.e. $h < a/2$, not shown here), the amplitude of the fluctuating lift decreases further, which affects the regularity in the time history of the lift force as the peaks of the fluctuating lift coefficient become irregular. When the particle gets very close to the wall (i.e. $h = a/20$, see Fig. 9c) the regular oscillation of the lift force disappears completely for all presented *Re* numbers, which is due to the formation of one single stable wake behind the particle.

Fig. 10 shows the effect of *Re* number on torque acting on the ellipse for different gap sizes. As shown in Fig. 6, for the ellipse

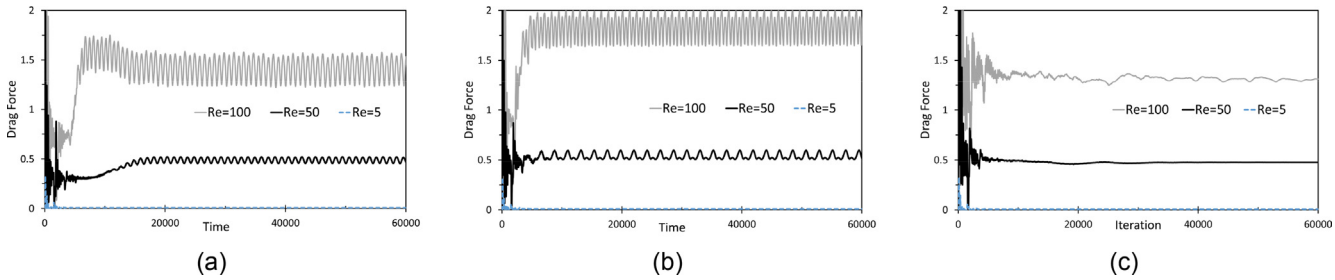

Fig. 8. Drag force acting on an ellipse with AR = 4, $\theta = 90^\circ$ at different *Re* numbers for (a) $h = 3a$, (b) $h = a/2$ and (c) $h = a/20$.

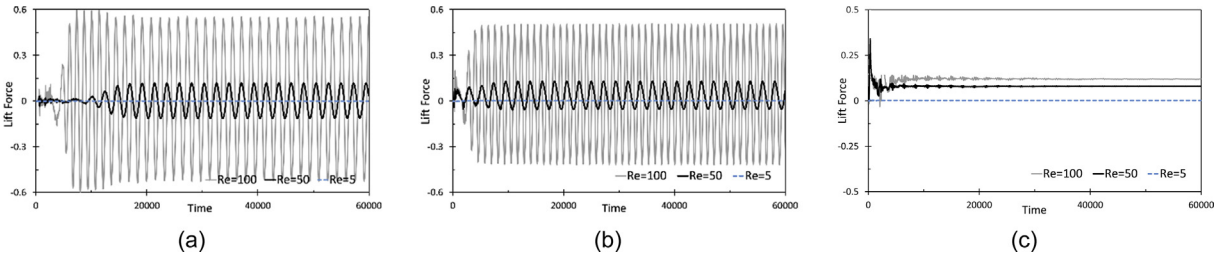

Fig. 9. Lift force acting on an ellipse with AR = 4, $\theta = 90^\circ$ at different *Re* numbers for (a) $h = 3a$, (b) $h = a/2$ and (c) $h = a/20$.

with $\theta = 90^\circ$, a large wake region is formed behind it. For all presented gap sizes, the size of the wake (i.e. stable recirculation region or shedding area) behind the ellipse increases in size as the *Re* number increases. As a result the pressure losses in the wake due to eddy formation increases. Consequently the pressure drag increases and becomes dominant compared to the viscous drag. When *Re* is small, the size of wake is small and the effect of the wall on the wake region is not high, resulting in a small torque acting on the ellipse. By increasing the *Re* number, the effect of symmetry breaking due to the existence of the wall become pronounced (even for lager gap size, $h = 3a$) and the magnitude of the torque increases.

As mentioned earlier, due to the existence of the wall the lower shear layer on the ellipse is interacting with the wall shear layer at relatively large gap ratios. This interaction is pronounced as the wake region becomes larger in size due to the increase in *Re* number. The negative wall shear layer cancels part of the vorticity in the positive lower shear layer of the ellipse, thus the lower shear layer is weakened. As a consequence, the separated positive lower shear layer is not strong enough, whereas the negative upper shear layer is strong enough to roll up to form a vortex. This phenomena results in a clockwise torque (i.e. with a negative sign) on the ellipse.

Moreover, it can be seen from Fig. 10 that for a fixed *Re* number, the magnitude of the rotation torque becomes smaller as the gap size reduces. As is clear from Fig. 7, by approaching the wall, the vortex shedding is suppressed due to the interaction between the wall and the ellipse shear layers which in turn results in a decrease in torque.

3.2.3. Orientation effect

The velocity vectors of fluid flow around an ellipse with AR = 4 and different orientations at *Re* = 100 are shown in Figs. 11–13 for $h = 3a$, $h = a/2$ and $h = a/20$, respectively. As is apparent from the figures, the flow is affected significantly by the particle orientation to the flow. It can be seen that when $\theta = 0^\circ$, a fixed pair of recirculation regions forms behind the ellipse and no vortex shedding is observed. In this case, the ellipse behaves as a streamlined body and the viscous (or friction) drag is the major contribution of the drag force.

By increasing the orientation angle, for $h = 3a$ and $a/2$ laminar vortex shedding is observed in which vortices are shed alternatively at either side of the ellipse at a certain frequency. By altering the orientation from $\theta = 0^\circ$ to 90°, the ellipse frontal size increases, the ellipse behaves like a bluff body which results in stronger vortex shedding. The larger the wake, the greater the pressure drag. The ellipse frontal size can act as an ultimate bluff body when its longer diameter is located perpendicular to the flow direction, i.e. $\theta = 90^\circ$. As the angle of attack increases between $\theta = 0^\circ$ and $\theta = 90^\circ$, a transition of streamlined body (viscous-drag dominant) to bluff body (pressure-drag dominant) occurs.

At $h = 3a$, the effect of the wall on vortex street is not high. However by decreasing the gap size to $h = a/2$, the wall may significantly affects the fluid flow for smaller orientation angles of the ellipse. For both $\theta = 30^\circ$ and $\theta = 150^\circ$, the lower shear layer on the ellipse merges completely with the wall shear layer and almost one-sided vortex shedding occurs. For the larger orientations (e.g. $\theta = 60^\circ$), the wall shear layer grows with the lower shear layer of the ellipse, and subsequently sweeps it away resulting in a vortex

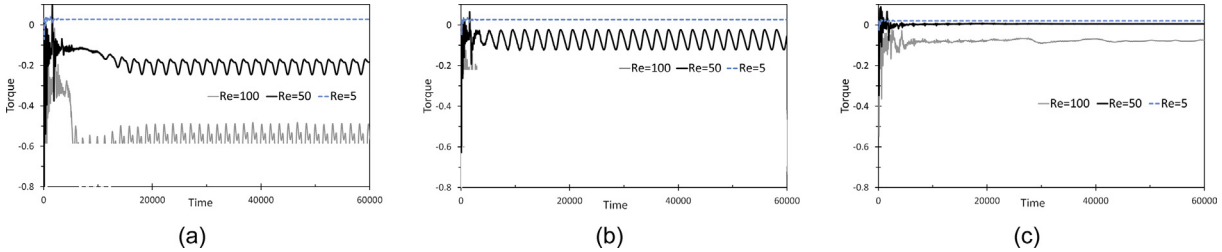

Fig. 10. Torque acting on an ellipse with AR = 4, $\theta = 90^\circ$ at different *Re* numbers for (a) $h = 3a$, (b) $h = a/2$ and (c) $h = a/20$.

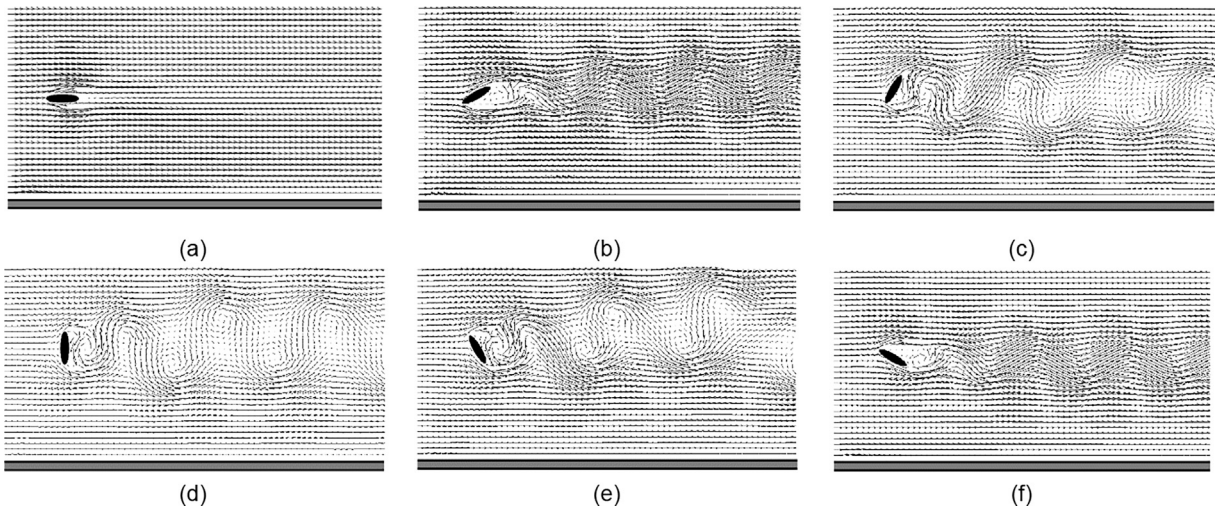

Fig. 11. Flow velocity vectors around an ellipse with AR = 4, *Re* = 100, *h* = 3a for (a) $\theta = 0°$, (b) $\theta = 30°$, (c) $\theta = 60°$, (d) $\theta = 90°$, (e) $\theta = 120°$ and (f) $\theta = 150°$.

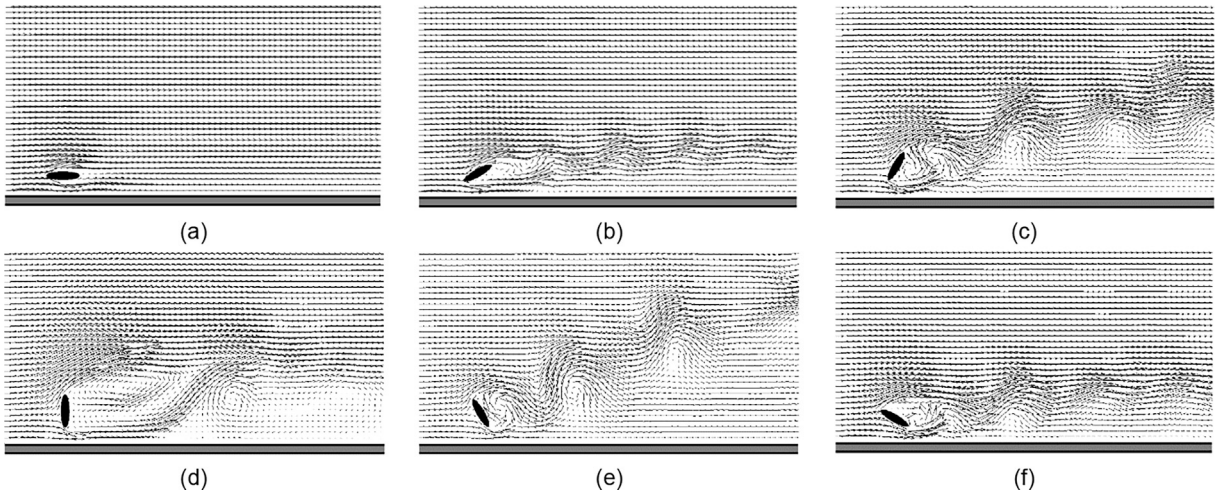

Fig. 12. Flow velocity vectors around an ellipse with AR = 4, *Re* = 100, *h* = a/2 for (a) $\theta = 0°$, (b) $\theta = 30°$, (c) $\theta = 60°$, (d) $\theta = 90°$, (e) $\theta = 120°$ and (f) $\theta = 150°$.

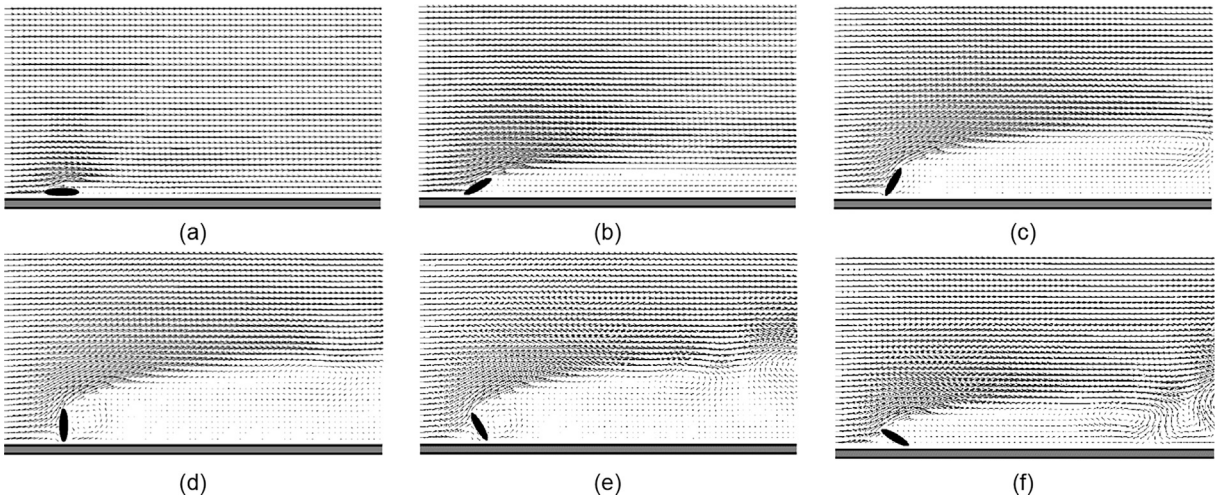

Fig. 13. Flow velocity vectors around an ellipse with AR = 4, *Re* = 100, *h* = *a*/20 for (a) $\theta = 0°$, (b) $\theta = 30°$, (c) $\theta = 60°$, (d) $\theta = 90°$, (e) $\theta = 120°$ and (f) $\theta = 150°$.

street inclined to the wall. At a very small gap size, i.e. $h = a/20$, the vortex shedding is suppressed for all orientations, the ellipse behaves like an obstacle to the fluid flow and altering the orientation just changes the size of the recirculation region behind the particle.

Fig. 14 shows the average of the drag and lift forces acting on an elliptical particle with AR = 4 and different orientation angle at $Re = 100$. Generally, the drag force is nearly constant at small angles (i.e. when $\theta \to 0°$ or $\theta \to 180°$). As the angle increases, the average drag quickly rises, for all presented gap sizes, because of increases frontal area and increase in boundary layer thickness. Also, it can be seen from Fig. 13(a) that the drag force increases as the gap size decreases from $h = 3a$ to $h = a$ due to the effect of the wall. However, by further decreasing the gap size to very small sizes the drag force decreases. As we discussed earlier in Section 3.2.2, the wall tends to slow down the gap flow at very small gap sizes which results in a reduction in viscous drag force.

The lift force crucially depends on the orientation of the particle relative to the fluid as its sign and magnitude changes significantly by changing the orientation angle (see Fig. 14(b)). One can see that the lift force acting on the particle for $\theta = 0°$ has a positive sign which directs the particle away from the wall. By increasing the orientation angle slightly (i.e. $0° < \theta < 90°$), the sign of lift force changes and becomes negative which represents a wall-directed lift force. By further increasing the orientation angle to $\theta > 90°$, the particle experiences a positive lift force again. These changes in the sign of the lift force are due to the orientation of the leading surface of the ellipse. When the orientation angle is $\theta < 90°$, a wake region with low pressure is formed behind the particle which results in a negative lift acting on the particle. This negative lift is added to the wall-directed lift force due to the accelerating gap flow near the wall, which together lead to a strong wall-directed lift force. By increasing the orientation angle to $\theta > 90°$, the particles becomes more and more streamlined subjected to the flow and the effect of wall-induced lift force due to the symmetry breaking of the wake flow becomes dominant that results in a positive lift force directed a way from the wall.

Also, it can be seen that from Fig. 14(b) that when $\theta < 90°$, the magnitude of the wall-directed lift force becomes larger by increasing the gap size, while for $\theta > 90°$ the maximum magnitude of lift force is observed when the gap size is the smallest. Generally for $\theta < 90°$, by increasing the gap size the low pressure region grows up and is pronounced which results in larger negative lift-force. However for $\theta > 90°$, the effect of the low pressure region is weakened due to the streamlining shape of the particle and the main wall-induced lift force is due to the symmetry breaking of vortices that are advecting from the particle surface. This symmetry breaking becomes stronger as the gap size decreases. As a result, by decreasing the gap size when $\theta > 90°$, the positive lift becomes pronounced.

The torque acting on the ellipse as a function of orientation angle is shown in Fig. 15. It can be seen that by increasing the orientation angle up to 90°, the particle experience a negative (clockwise) torque. The reason is that the shear layer on the lower surface of the particle interacts with the shear layer of the wall with the negative sign and cancel out each other to some extent (depending on the gap size). Hence, the shear layer on the upper side of the ellipse with a negative sign is the dominant phenomenon that results in a clockwise rotation of the particle. For θ >90°, the ellipse experiences a positive lift and drag forces leading to positive counter clockwise torque.

3.2.4. Aspect Ratio effect

To show the effect of aspect ratio on flow structures, velocity contour plots and vectors are shown in Fig. 16 for flow around an ellipse with $\theta = 90°$, $h = a$, $Re = 25$ and different AR. As is apparent from Fig. 16, the flow structure changes by varying the AR, as a steady-state wake region is observed behind the ellipse with AR = 1 and 2, whereas for AR = 3 and 4 the time-dependent vortex shedding is formed behind the ellipse. Fig. 17 shows the flow velocity vectors around an ellipse with AR = 1 and 4 when $\theta = 0°$ (or 180°), $h = 2a$ and $Re = 100$. It is evident that by changing the orientation angle, the cross-section and the resistance of the ellipse against the flow changes and, as a result, the structure of wake region changes. By increasing the AR when $\theta = 0°$, the ellipse becomes more streamlined, and consequently, the wake region remains steady-state, whereas the vortex shedding is visible for AR = 1.

Fig. 18 shows the drag and lift forces and also torque acting on an elliptical particle with different aspect ratios and different

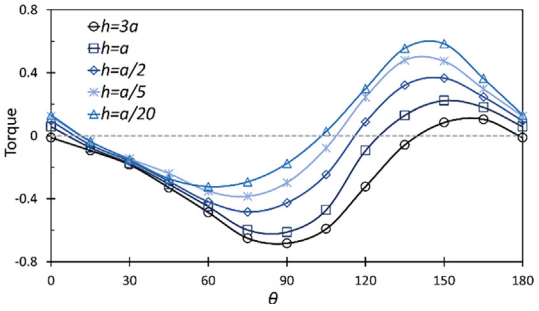

Fig. 15. Torque as a function of orientation angle, θ, for an elliptic particle with AR = 4 and $Re = 100$.

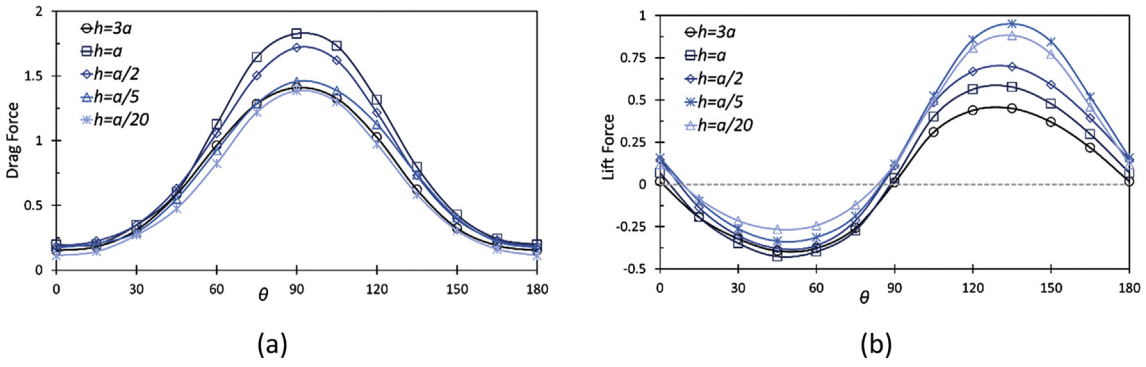

Fig. 14. The average of the (a) drag and (b) lift forces as a function of orientation angle, θ, for an elliptic particle with AR = 4 and $Re = 100$.

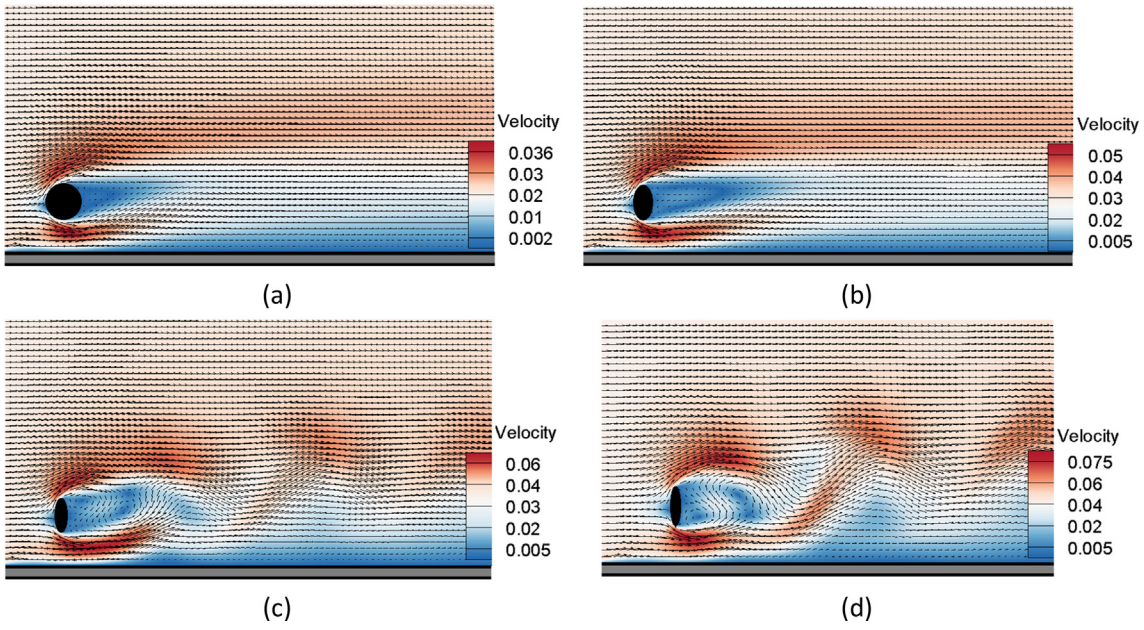

Fig. 16. Flow velocity vectors around an ellipse with $\theta = 90°$, $h = a$, $Re = 25$ for (a) AR = 1, (b) AR = 2, (c) AR = 3 and (d) AR = 4.

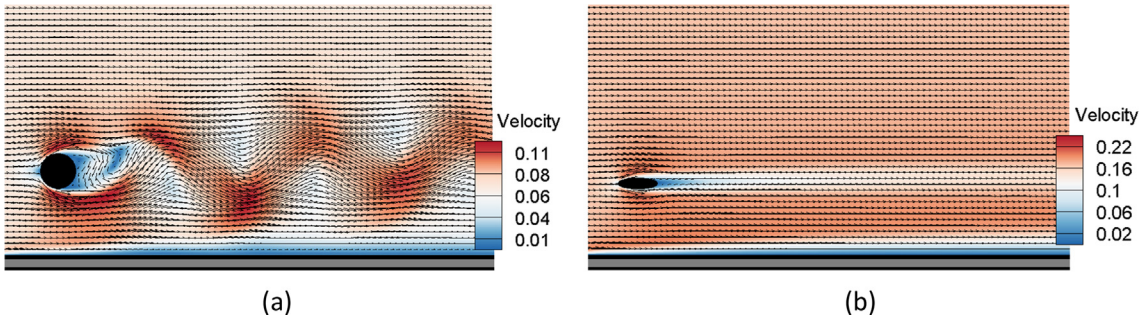

Fig. 17. Flow velocity vectors around an ellipse with $\theta = 0°$, $h = 2a$, $Re = 100$ for (a) AR = 1, (b) AR = 4.

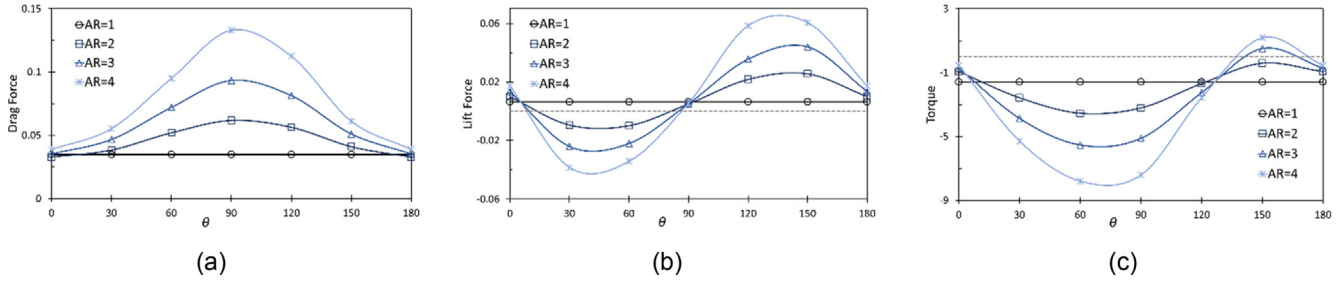

Fig. 18. (a) Drag force, (b) lift force and (c) torque as a function of orientation angle, θ, for an elliptic particle with various aspect ratios (AR), $h = a$ and $Re = 25$.

orientation angles with $h = a$ and $Re = 25$. It is evident from Fig. 18 (a) that a particle with higher AR is subjected to larger drag force when $0° < \theta < 180°$ whatever the gap size. As it was shown in Fig. 16, by increasing the AR the wake behind the ellipse grows more quickly and vortex shedding occurs sooner and as a result, the pressure drag becomes the main contribution to the drag force resulting in increases in the drag force. However, this trend is different for an ellipse with $\theta = 0°$ (or 180°). As shown in Fig. 17, the ellipse with larger AR and $\theta = 0°$ becomes more streamlined, vortex shedding is suppressed and the viscous drag grows to be the main contribution to the drag force. Hence, the drag force decreases when AR increases from 1 to 2 due to the vanishing of the vortex shedding. By further increasing the AR to 3 and 4, the flow remains attached to the surface of the ellipse and the viscous drag is pronounced, resulting in an increase in the drag force.

Fig. 18(b) and (c) show that an ellipse with higher AR experiences larger lift and torque. The magnitude of lift and torque increases for increasing AR whatever the gap size and orientation angle. However, the inflection points for lift and torque are $\theta = 90°$ and $\theta = 0°$ (or $\theta = 180°$), respectively. When $\theta = 90°$ (or $\theta = 0°$), the particle with higher AR is subjected to lower lift (or torque) which is due to the effect of incidence angle, as expected.

4. Conclusion

The lattice Boltzmann method was used to perform numerical simulations for a detailed investigation of the effects of a solid wall on drag, lift and rotation torque acting on a fixed non-spherical (elliptical) particle. The effect of gap size, particle Reynolds number and particle orientation were studied. The numerical results showed that the presence of a wall significantly changes the flow field and resulting hydrodynamic forces, as an increase or decrease of the drag and lift forces depend on the gap size. Also the direction of lift (i.e. wall-directed or directed a way from the wall) and torque (i.e. clockwise or counter clockwise) change depending on both the gap size and particle orientation angle. Also, our results showed that an ellipse with higher AR usually experiences larger hydrodynamic forces and torque whatever the gap size and orientation angle.

Acknowledgement

This work was done as a part of research funded by the European Research Council (ERC) under the consolidator grant scheme, contract no. 615096 (NonSphereFlow).

References

[1] S. Torquato, F.H. Stillinger, Jammed hard-particle packings: from Kepler to Bernal and beyond, Rev. Mod. Phys. 82 (2010) 2633–2672.
[2] G. Seiden, P.J. Thomas, Complexity, segregation, and pattern formation in rotating-drum flows, Rev. Mod. Phys. 83 (2011) 1323–1365.
[3] M. Amutio, G. Lopez, M. Artetxe, G. Elordi, M. Olazar, J. Bilbao, Influence of temperature on biomass pyrolysis in a conical spouted bed reactor, Resour. Conserv. Recycl. 59 (2012) 23–31.
[4] B. Ren, W. Zhong, B. Jin, Y. Shao, Z. Yuan, Numerical simulation on the mixing behavior of corn-shaped particles in a spouted bed, Powder Technol. 234 (2013) 58–66.
[5] W. Zhong, A. Yu, X. Liu, Z. Tong, H. Zhang, DEM/CFD-DEM modelling of non-spherical particulate systems: theoretical developments and applications, Powder Technol. 302 (2016) 108–152.
[6] P. Decuzzi, R. Pasqualini, W. Arap, M. Ferrari, Intravascular delivery of particulate systems: does geometry really matter?, Pharm Res. 26 (1) (2009) 235–243.
[7] D. Hohner, S. Wirtz, V. Emden, H.K. Scherer, Comparison of the multi-sphere and polyhedral approach to simulate non-spherical particles within the discrete element method, Powder Technol. 208 (2011) 643–656.
[8] L. Yang, J.T. Padding, J.A.M. Hans Kuipers, Investigation of collisional parameters for rough spheres in fluidized beds, Powder Technol. 316 (2017) 256–264.
[9] Z. Zhou, G. Jin, B. Tian, J. Ren, Hydrodynamic force and torque models for a particle moving near a wall at finite particle Reynolds numbers, Int. J. Multiphase Flow 92 (2017) 1–19.
[10] H. Lee, S. Balachandar, Effects of wall roughness on drag and lift forces of a particle at finite Reynolds number, Int. J. Multiphase Flow 88 (2017) 116–132.
[11] G. Bagheri, C. Bonadonna, I. Manzella, P. Vonlanthen, On the characterization of size and shape of irregular particles, Powder Technol. 270 (2015) 141–153.
[12] G. Bagheri, C. Bonadonna, On the drag of freely falling non-spherical particles, Powder Technol. 301 (2016) 526–544.
[13] S.K.P. Sanjeevi, J.T. Padding, On the orientational dependence of drag experienced by spheroids, J. Fluid Mech. 820 (2017) R1.
[14] M. Zastawny, G. Mallouppas, F. Zhao, B. Van Wachem, Derivation of drag and lift force and torque coefficients for non-spherical particles in flows, Int. J. Multiphase Flow 39 (2012) 227–239.
[15] R. Ouchene, M. Khalij, B. Arcen, A. Tanière, A new set of correlations of drag, lift and torque coefficients for non-spherical particles and large Reynolds numbers, Powder Technol. 303 (2016) 33–43.
[16] C. Yin, L. Rosendahl, S.K. Kær, T.J. Condra, Use of numerical modeling in design for co-firing biomass in wall-fired burners, Chem. Eng. Sci. 59 (2004) 3281–3292.
[17] L. Zeng, F. Najjar, S. Balachandar, P. Fischer, Forces on a finite-sized particle located close to a wall in a linear shear flow, Phys. Fluids 21 (3) (2009) 033302.
[18] F. Takemura, J. Magnaudet, The transverse force on clean and contaminated bubbles rising near a vertical wall at moderate Reynolds number, J. Fluid Mech. 495 (2003) 235–253.
[19] L. Zeng, S. Balachandar, P. Fischer, Wall-induced forces on a rigid sphere at finite Reynolds number, J. Fluid Mech. 536 (2005) 1–25.
[20] A.J. Goldman, R.G. Cox, H. Brenner, Slow viscous motion of a sphere parallel to a plane wall – I Motion through a quiescent fluid, Chem. Eng. Sci. 22 (1967) 637–651.
[21] E. Gavze, M. Shapiro, Particles in a shear flow near a solid wall: effect of nonsphericity on forces and velocities, Int. J. Multiphase Flow 23 (1) (1997) 155–182.
[22] S.Y. Lee, J.Y. Hyun, Analysis of force acting on the non-spherical particle near a wall, Biomed. Eng. Lett. 5 (4) (2015) 289–295.
[23] M.A. Rizk, S.E. Elghobashi, The motion of a spherical particle suspended in a turbulent flow near a plane wall, Phys. Fluids 28 (3) (1985) 806–817.
[24] H. Lee, S. Balachandar, Drag and lift forces on a spherical particle moving on a wall in a shear flow at finite *Re*, J. Fluid Mech. 657 (2010) 89–125.
[25] T. Tsuji, E. Narita, T. Tanaka, Effect of a wall on flow with dense particles, Adv. Powder Technol. 24 (2) (2013) 565–574.
[26] S. Succi, The Lattice Boltzmann Equation for Fluid Dynamics and Beyond, Oxford Univ Press, 2001.
[27] S. Mukherjee, A. Zarghami, C. Haringa, K. van As, S. Kenjereš, H.E.A. Van den Akker, Simulating liquid droplets: A quantitative assessment of lattice Boltzmann and Volume of Fluid methods, Int. J. Heat Fluid Flow 70 (2018) 59–78.
[28] A. Zarghami, S. Ubertini, S. Succi, Finite volume formulation of thermal lattice Boltzmann method, Int. J. Numer. Method H. 24 (2) (2014) 270–289.
[29] A. Zarghami, H.E.A. Van den Akker, Thermohydrodynamics of an evaporating droplet studied using a multiphase lattice Boltzmann method, Phys. Rev. E 95 (4) (2017) 043310.
[30] A.J.C. Ladd, Numerical simulations of particulate suspensions via a discretized Boltzmann equation, part 2. Numerical results, J. Fluid Mech. 271 (1994) 311–339.
[31] M. Bouzidi, M. Firdaouss, P. Lallemand, Momentum transfer of a Boltzmann lattice fluid with boundaries, Phys. Fluids 13 (11) (2001) 3452–3459.
[32] X. He et al., Analytic solutions of simple flows and analysis of nonslip boundary conditions for the lattice Boltzmann BGK model, J. Stat. Phys. 87 (1997) 115–136.
[33] T. Krüger, The Lattice Boltzmann Method, Springer, 2017.
[34] P. Lallemand, L.S. Luo, Pierre Lallemand, Li-Shi Luo, Theory of the lattice Boltzmann method: Dispersion, dissipation, isotropy, Galilean invariance, and stability, Phys. Rev. E 61 (6) (2000) 6546.
[35] Q. Zou, X. He, On pressure and velocity boundary conditions for the lattice Boltzmann BGK model, Phys. Fluids 9 (1997) 1591–1598.
[36] I. Orlanski, A simple boundary condition for unbounded hyperbolic flows, J. Comput. Phys. 21 (3) (1976) 251–269.
[37] Q. Lou, Z. Guo, B. Shi, Evaluation of outflow boundary conditions for two-phase lattice Boltzmann equation, Phys. Rev. E 87 (6) (2013) 063301.
[38] H. Schlichting, Boundary-Layer Theory, McGraw-Hill, 1968.
[39] L.-S. Luo et al., Numerics of the lattice Boltzmann method: effects of collision models on the lattice Boltzmann simulations, Phys. Rev. E 83 (2011) 056710.
[40] T. Ye, R. Mittal, H. Udaykumar, W. Shyy, An accurate cartesian grid method for viscous incompressible flow with complex immersed boundaries, J. Comput. Phys. 156 (1999) 209–240.
[41] S.C.R. Dennis, G.Z. Chang, Numerical solutions for steady flow past a circular cylinder at Reynolds numbers up to 100, J. Fluid Mech. 42 (3) (1970) 471–489.
[42] M.C. Thompson, T. Leweke, M. Provansal, Kinematics and dynamics of sphere wake transition, J. Fluids Struct. 15 (2001) 575–585.
[43] M. Provansal, L ., chouveiler, T. Leweke, From the double vortex street behind a cylinder to the wake of a sphere, Eur. J. Mech. B-Fluid 23 (1) (2004) 65–80.